Experimental and numerical analyses of stiffness and fatigue properties of a spring element for mounts with tunable stiffness made of C85S+QT sheet steel

Volker Landersheim, Cedric Mathieu, Jan Hansmann, William Kaal
Fraunhofer Institute for Structural Durability and System Reliability LBF, Germany
volker.landersheim@lbf.fraunhofer.de, https://orcid.org/0000-0002-0877-7899
cedric.mathieu@lbf.fraunhofer.de, https://orcid.org/0009-0008-0468-9681
jan.hansmann@lbf.fraunhofer.de, https://orcid.org/0009-0008-9375-4499
william.kaal@lbf.fraunhofer.de, https://orcid.org/0000-0002-7526-3599

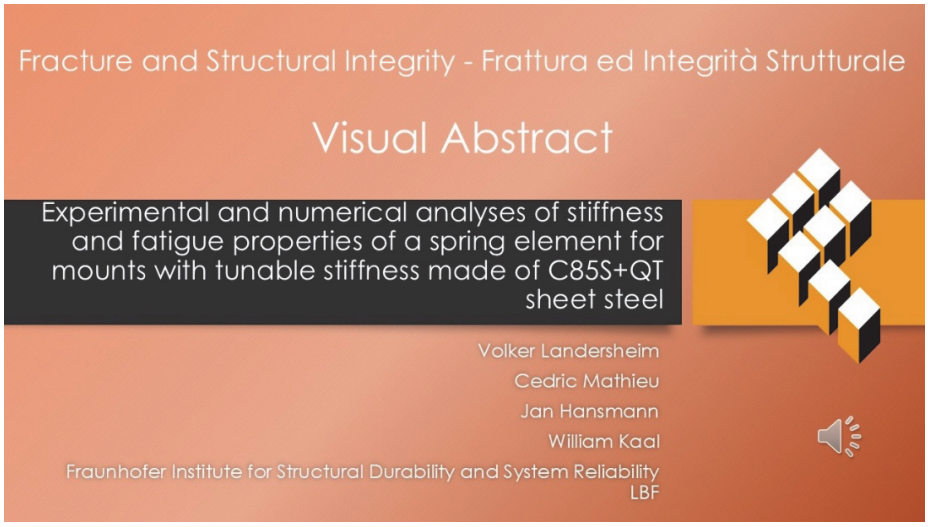

Citation: Landersheim, V., Mathieu, C., Hansmann, J., Kaal, W., Fatigue properties of a spring element for mounts with tunable stiffness made of C85S+QT sheet steel, Fracture and Structural Integrity, 75 (2026) 297-314.

Received: 20.08.2025
Accepted: 29.09.2025
Published: 12.11.2025
Issue: 01.2026

KEYWORDS. Stiffness, Fatigue, Tunable mounts, S-N curve, Component test, FEA.

INTRODUCTION

The performance of many technical systems depends on some kind of stiffness inside the respective system. For example, the ride dynamics of a vehicle strongly depend on the stiffness and damping setup of the chassis [1], the accuracy of robot based milling processes is limited by the mechanical resonance frequency of the system [2], and the efficiency of a rotational energy harvesting vibration absorber depends on the correct tuning which is – among other parameters – defined by the rotational stiffness of the system [3].

For research and development tasks in particular, it is beneficial if local stiffnesses of a test setup can be changed fast and with low effort, e.g. in form of a tunable mount. This allows efficient R&D, e.g. to collect training data for different mounting scenarios of a device under test or to do experimental sensitivity studies.
There are different modes of action which allow the realization of a tunable stiffness. Tab. 1 gives an overview with some examples.

Mode of action	Examples
Mechanical tuning	Varying basic geometric parameters that influence stiffness, e.g. changing the length of a beam [4] or use of gears [5], jamming structures [6], or lever mechanisms [7]
Smart Materials	Shape memory alloys [8], Low Melting Point Alloys [9], Piezoceramics [10], Magnetorheological elastomers [11]
Fluid based	Compressible fluids like air in a defined chamber as spring element which can be tuned e.g. by change of pressure or chamber dimensions [12]

Table 1: Different modes of action to realise an element with tunable stiffness.

From an application point of view, it is desirable to have a simple and reliable solution to realise a tunable stiffness function. Therefore, Fraunhofer LBF has developed a mechanism which allows stiffness tuning in a broad range and falls under the principle of mechanical stiffness tuning. Fig. 1 shows the basic principle of this stiffness tuning mechanism, which is based on the idea of changing the length of a bending beam. It consists of an inner and an outer component, which are connected by a spring element orientated along a circular path. The clamping position of the outer component, defined by the angle φ, determines the effective length of the spring arms and therefore the axial stiffness of the mount.

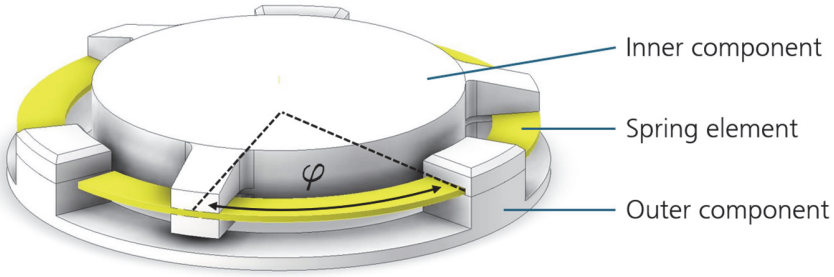

Figure 1: Components and basic principle of the tunable stiffness mechanism.

This stiffness tuning mechanism allows the realization of tunable mounts, Fig. 2 shows an example. Regarding tasks in research and development there are several examples where it is crucial to suspend or mount specimens with a certain stiffness.

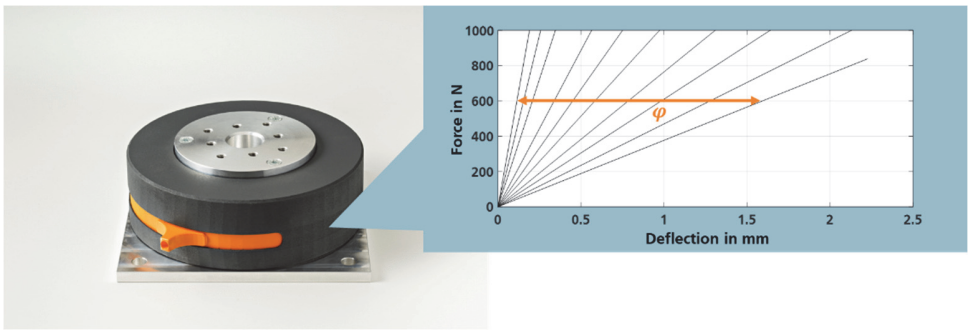

Figure 2: Mount with tunable stiffness (left) and force-deflection measurements for different settings (right).

Therefore, the mechanism shown in Fig. 1 is used for stiffness tuning in several applications, e.g.: investigations on joining processes, where the process parameters depend on the stiffness of the parts to be joined [13], the active emulation of vehicle body stiffness to consider non-linear effects of the chassis suspension in NVH investigations [14], the mounting of

a test piece to achieve a defined strain distribution in durability testing [15], for example for the durability testing of structurally integrated high voltage systems of vehicles [16].
Especially when it comes to experimental research in the field of durability testing, it is crucial that the tunable devices fulfill certain durability requirements. Therefore, the durability of the beforehand described mechanism has been investigated with a combined approach consisting of experimental durability tests, an analytical description, and numerical modeling.
The following section, 'Methods', describes the design of the stiffness element under investigation, how it was modelled for FE analysis, and how the test setup for the fatigue tests was configured. The section 'Results' presents the results of the fatigue tests and the FE-based stress analysis of the test configurations. The subsequent section proposes an approximation approach intended to enable a quick preliminary estimation of stiffness and fatigue strength using analytical equations only.

METHODS

Tunable stiffness element under investigation

A single spring element with three arms was used as specimen for the investigations, see Fig. 3. The springs were made from hardened spring steel sheets (C85S+QT (material number 1.1269)). According to the manufacturer's specifications, the tensile strength of the material is between 1320 and 1520 N/mm². They are manufactured with a thickness of 1.5 mm and 3 mm by water jet cutting. Furthermore, the angles $\varphi = 30°$ and $\varphi = 100°$, i.e. a rather stiff and a rather soft setting, were selected for the tests. Fig. 3 shows the detailed geometry and dimensions of the test specimens including spring arm, spacer and slider.

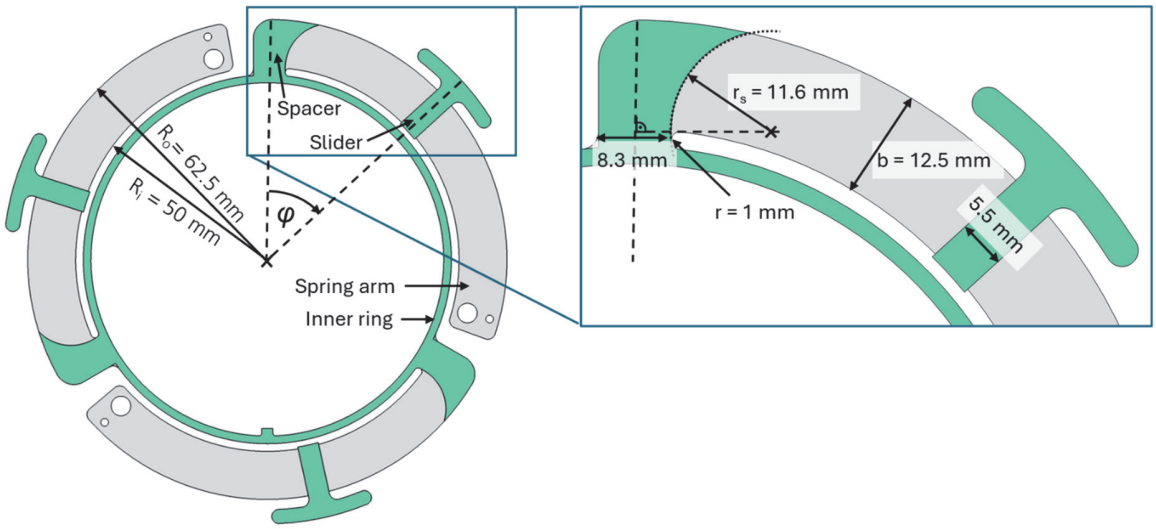

Figure 3: Dimensions of the test specimens with three spring arms, spacers and sliders.

Used models of the stiffness element

The stiffness as well as the local notch stresses are analysed by FE analysis of the system consisting of spring arm, spacer and slider. The model shown in Fig. 4 for the case of a spring arm with a thickness of $t = 3$ mm and spacers of the same thickness.
The colours in the figure represent the distribution of displacement in the axial direction when applying an axial displacement of 1 mm at the slider. For the contact between spring arm and spacer as well as between spring arm and slider a frictionless contact with linear normal stiffness is used. A rigid boundary condition is applied to the spacer at its connection to the inner ring. For the slider, a boundary condition is applied, which allows only movement in the axial direction.
Fig. 5 shows a more detailed view on the mesh geometry at the notch for the spring arm with a thickness of $t = 1.5$ mm. For all test cases, the notch geometry was meshed with four elements in the thickness direction of the spring arm and twelve elements in the circumferential direction of the notch radius using quadratic brick elements (Abaqus C3D20).

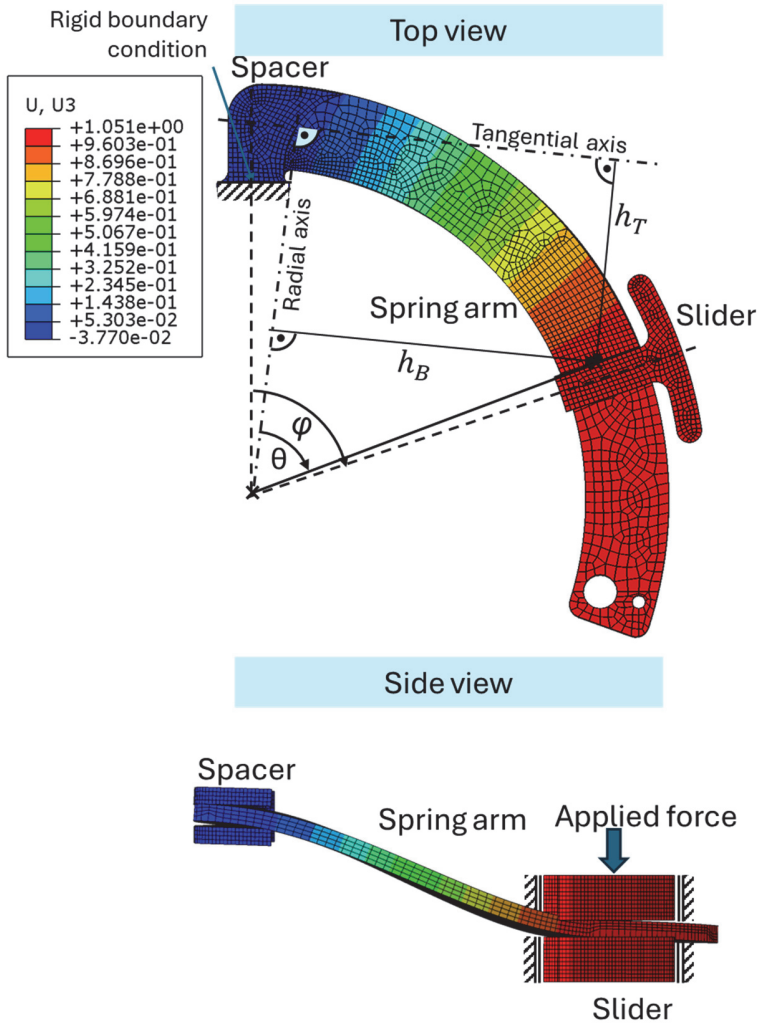

Figure 4: FE model of the system consisting of spring arm, spacer and slider. (Example with an angle of φ = 70°) and spring arm thickness t = 3 mm.)

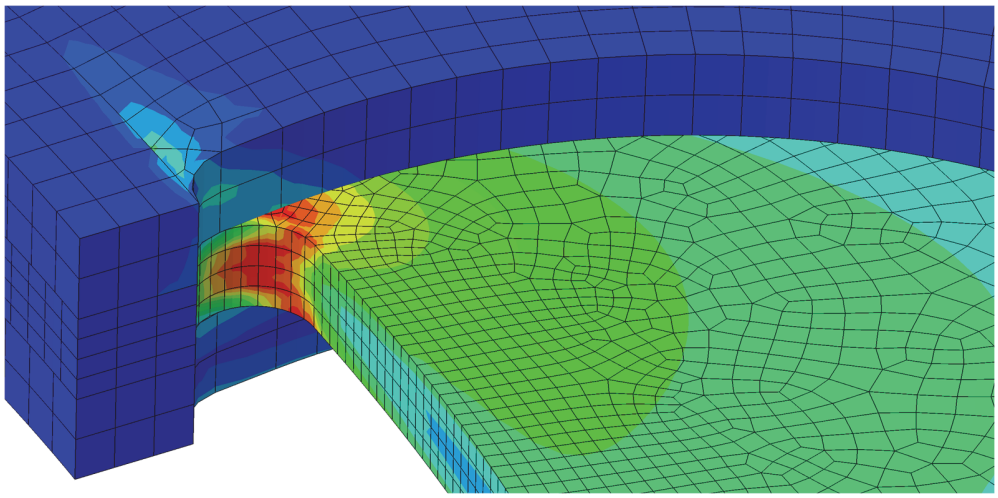

Figure 5: Details view of the mesh geometry at the notch for the spring arm with a thickness of t = 1.5 mm.

Test setup for fatigue tests

Fatigue strength tests were carried out to determine the durability of the spring elements under cyclic loading. This also provides a basic understanding of the failure mechanism and the dependency of the spring characteristics on the progress of the damage. Four load-life curves were determined experimentally, whereby the parameters spring sheet thickness t and slider position angle φ were varied. Nine specimens were used for each load-life curve.

The test setup for the fatigue tests is shown in Fig. 6 (left); a photo of the technology demonstrator in the installed state is shown on the right. To apply loads to the springs, the inner part of the clamping device was deflected using a hydraulic cylinder (Sandner SLZ40-40S servo cylinder) and a force application rod. The opposite side was fixed to the load frame via a load cell (Interface 1720ACK-10kN). The tunable mounts were sinusoidally loaded with a load ratio of R = -1 under displacement control, which used the signal from the LVDT displacement sensor integrated in the hydraulic cylinder (control system: MTS FlexTest 60).

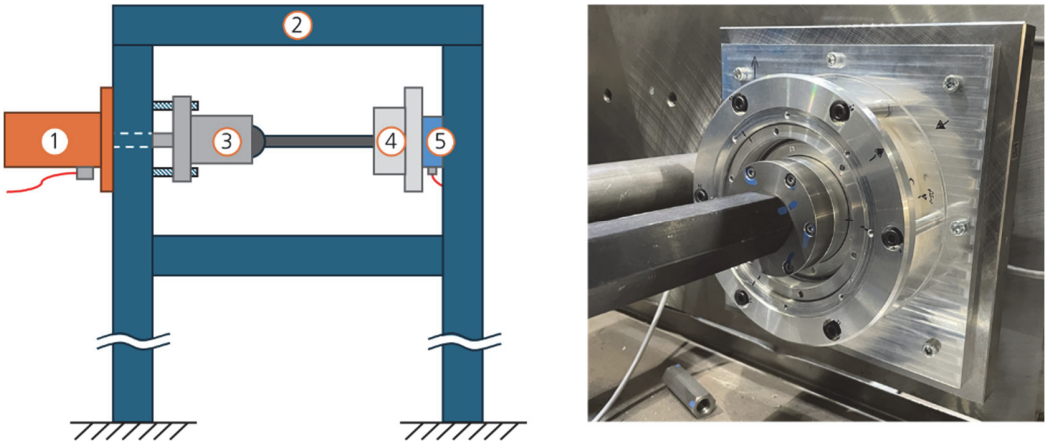

Figure 6: Left: Schematic representation (not to scale) of the test rig used to test the spring elements with the components hydraulic cylinder (1), load frame (2), rod with ball joint (3), clamping device with spring element (4) and load cell (5). Right: Installed specimen.

The degradation of the springs is particularly noticeable through a drop in spring stiffness. With the installed load cell, this was monitored using the development of the force amplitude over the number of load cycles, whereby the percentage drop in force in relation to the amount at the start of the test was used as the failure criterion, see next section. As an example, the trend curves of the force maxima for the test series with the parameter combination thickness of 3 mm and angle of 30° are shown in Fig. 7. The degradation of the specimens as a result of cyclic damage is clearly noticeable in the decrease in the force maxima with increasing number of load cycles.

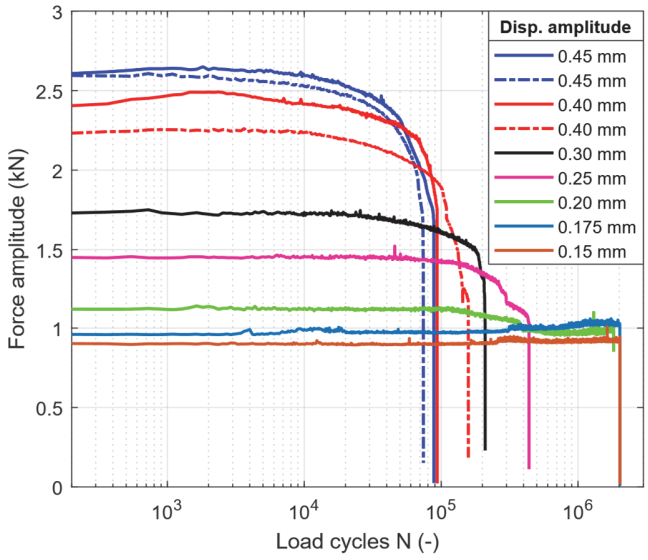

Figure 7: Fatigue behavior of the spring elements as a function of the displacement amplitude.

No failure occurred at amplitudes of 0.15 and 0.175 mm; the sudden decrease at the end of these curves is due to the automatic switch-off of the test bench after two million cycles. For the other specimens, a decrease in stiffness up to component failure can be observed. With some specimens, discontinuities in the degradation velocity can be observed, e.g. at around $3 \cdot 10^5$ cycles for the specimen with 0.25 mm amplitude. This may be due to the fact that testing this spring geometry involves a parallelised test with three spring arms, which are loaded identically but can fail at different times. With the one load cell used, only the summed force of all spring arms is measured. Hence, only the stiffness decrease of the spring as a whole, based on its value after the run-in phase of the experiment, was taken into account for the failure criterion.
The permissible service life of the mounts depends largely on the selected failure criterion. To illustrate this influence, Fig. 8 shows the service lives for several limit values of the stiffness drop for the example of the specimen with a thickness of t = 3 mm and angle φ = 30°.

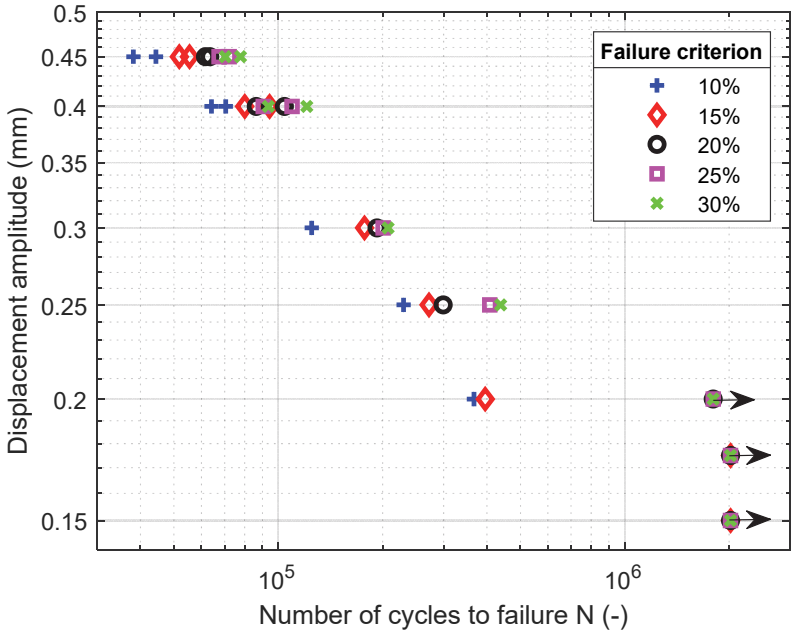

Figure 8: Fatigue life as a function of displacement amplitude and the failure criterion. The latter refers to the relative drop in spring stiffness due to damage during the experiments.

Since the purpose of the tunable mounts is to provide a defined stiffness, only the data points generated with the 10% stiffness drop criterion are used in the following analyses.
As a further termination criterion for the experiments, a limit number of load cycles of two million cycles was defined and everything above this was labelled as runout.

RESULTS

Experimental results

The average stiffnesses of the undamaged springs are listed for each tested parameter combination in Tab. 2.
During loading, the spring arms are subjected to high stresses, particularly at the notch radius between the spring arm and the inner ring as well as at the clamping by the sliders. Fig. 9 shows the typical damage pattern occurring at the notch: starting from the notch, a crack has formed that is orientated radially outwards and is continuous in the thickness direction, which has led to the almost complete separation of the spring arm.
Of the 36 springs tested, 27 failed primarily due to partial or complete separation of one or more spring arms at the notch, while two springs failed primarily due to failure at the clamping. The remaining seven test specimens did not suffer any damage at their respective load amplitudes.
These data points are summarised in Fig. 10 together with the corresponding load-life curve based on these data points.

Thickness t (mm)	Angle φ (°)	Stiffness (N/mm)
1.5	30	1083 ± 35
1.5	100	40.23 ± 0.86
3.0	30	5831 ± 137
3.0	100	262.2 ± 5.6

Table 2: Average spring stiffness of the tested springs per sheet thickness and angular position of the slider.

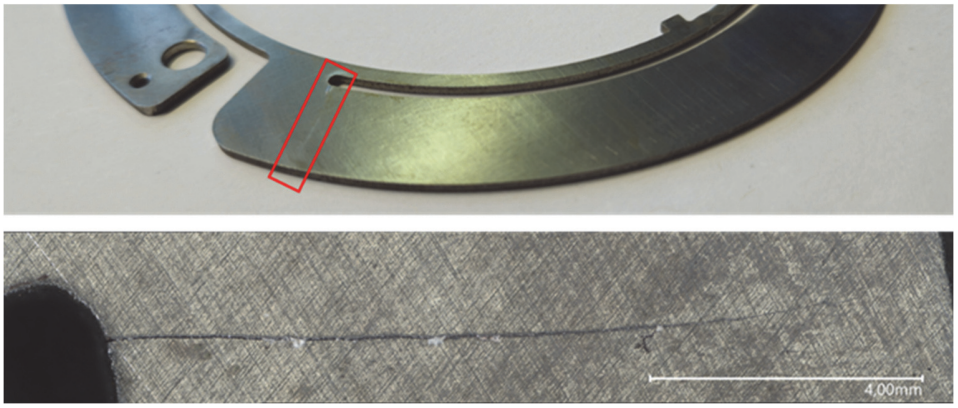

Figure 9: Picture of a test specimen with a cracked spring arm (top). Microscopic image of the section marked in red (bottom) with a clearly recognizable crack along the width of the spring.

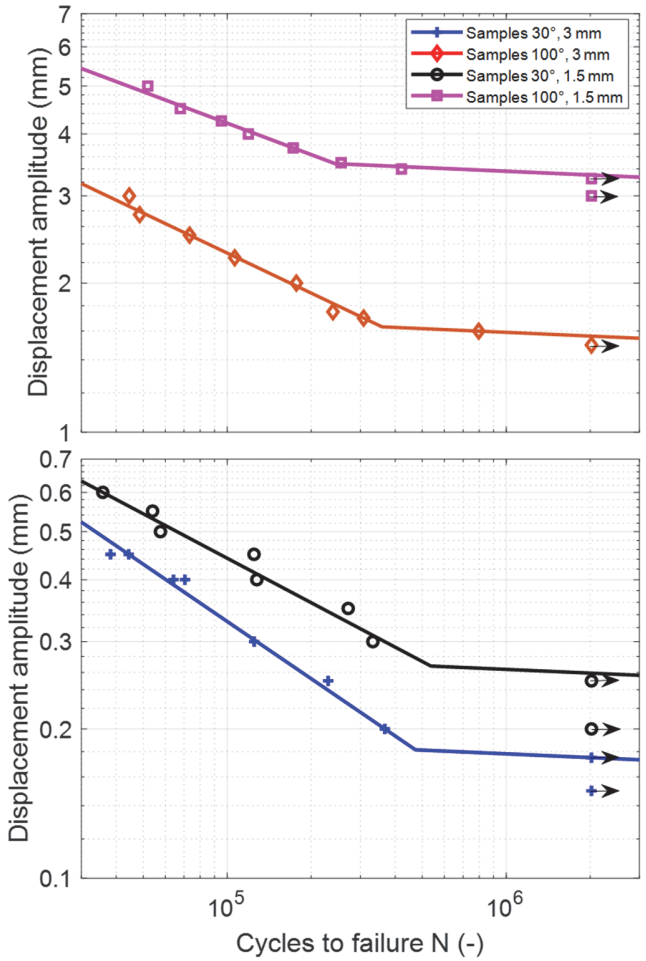

Figure 10: Load-life curves of the four test series (failure criterion 10% reduction in force).

The results of the fatigue tests are used to calibrate numerical models for assessing the fatigue strength, see next sections.

Results of FE based stress estimation

The experimental fatigue results can be used for an FE-based fatigue assessment of other configurations of the tunable stiffness device then the ones under test. But this requires knowledge of the component related material strength at the notch root. For this purpose, the notch stresses for the four test cases have been computed using the FE model depicted in Fig. 4.

Fig. 11 shows the S-N-diagram for all test samples with the experimentally derived fatigue life (Criterion: 10% reduction in force) and the maximum Mises stress at the notch computed with the FE models.

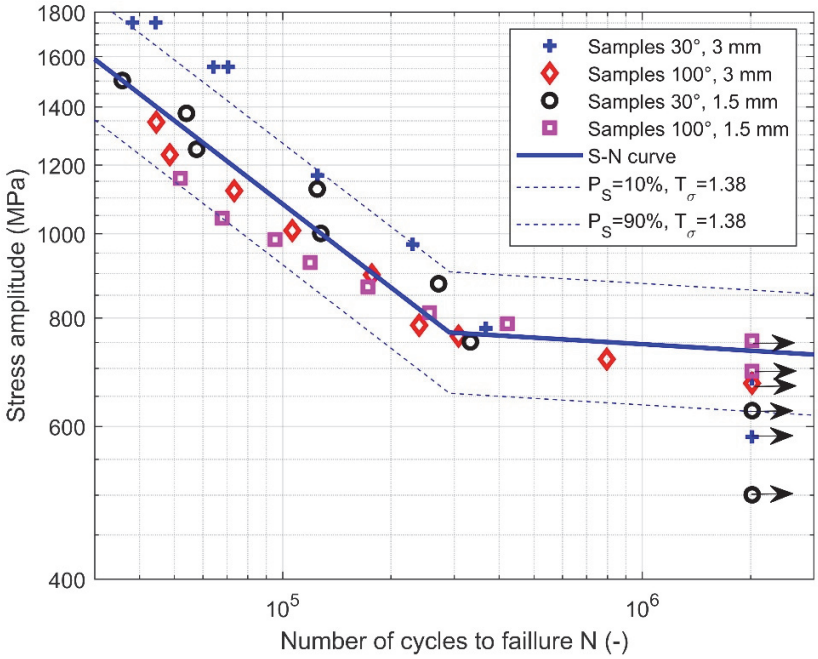

Figure 11: S-N-curve for notch stresses (Mises) derived using FE stress analysis for experimental test cases.

The S-N curve depicted in this figure has an inclination of k = 3.13, a knee-point of N_k = 291 000 cycles and a stress amplitude at the knee-point of σ_k = 769.7 MPa. 80% of the samples are within a scatter band with a width of T_σ = 1.38. This S-N curve can be used for an FE based fatigue analysis for spring arms from the same material with a similar geometry using the same meshing parameters. If the sheet thickness, notch radius or notch geometry differ in the order of magnitude from the ones in this investigation, also size effects need to be considered [17, 18, 19, 20].

APPROXIMATION APPROACH FOR STIFFNESS AND FATIGUE STRENGTH

For the design of tunable mounts, their stiffness and strength are determined using FE-based approaches in the design phase. Requirements regarding the size of the device have to be defined beforehand. Typically, the design process starts with requirements like a stiffness range and acceptable displacements and loads for the device. For an efficient optimization of the geometric parameters for pre-dimensioning, their effect on stiffness and strength must be estimated before an FE model of the device exists.

Stiffness estimation

The average stiffnesses of the analysed configurations determined in the tests (see Tab. 2) represents the total stiffness k_{tot} of the structure under test. This total stiffness can be approximated as a series connection of several elasticities as in Eqn. 1.

$$k_{tot} = 1/\left(\frac{1}{k_{sa}} + \frac{1}{k_s} + \frac{1}{k_{fts}}\right) \tag{1}$$

Firstly, there is the stiffness k_{sa} of the spring arm itself, which is subjected to a combined torsional and bending load. Its connection via the spacers to inner ring of the device forms an elastic clamping of the spring arm with the stiffness k_s. Finally, the other force-transmitting components in the structure also have a finite stiffness denoted by k_{fts}.

The stiffness of the spring arm k_{sa} can be described using the equations of mechanics for the elastic deformation of curved beams[21], assuming an ideal rigid clamping on one end of the curved beam, and only a translational degree of freedom in the axial direction on the other end, see Fig. 12.

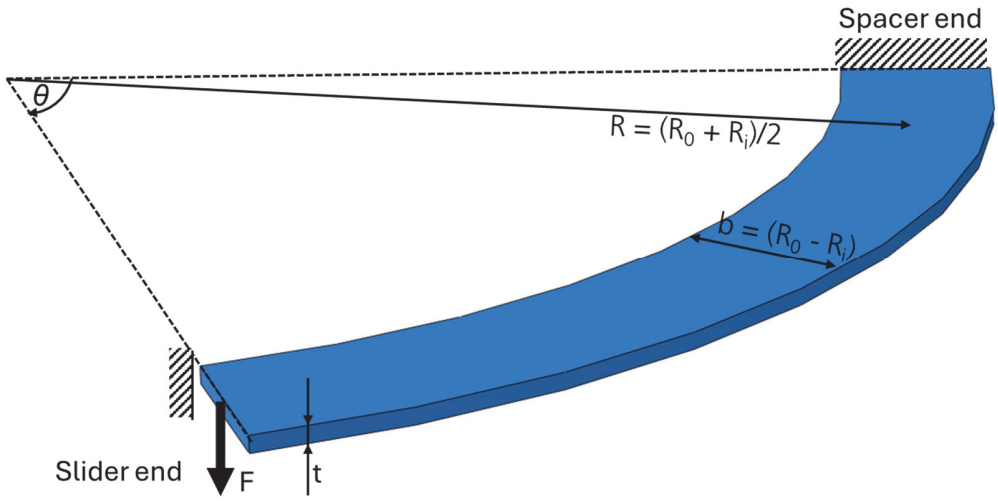

Figure 12: Idealised curved bending arm.

This algebraic description is given in Eqn. 2.

$$k_{sa} = 1/\left[\frac{R^3}{EI}\left(-\left(\frac{A_2}{A_5} - \frac{\frac{A_1}{A_5} - \frac{A_2 A_4}{A_5^2}}{1-\left(\frac{A_6 A_4}{A_5^2}\right)}\frac{A_6}{A_5}\right)A_1 - \frac{\frac{A_1}{A_5} - \frac{A_2 A_4}{A_5^2}}{1-\left(\frac{A_6 A_4}{A_5^2}\right)}A_2 + A_3\right)\right] \tag{2}$$

The following abbreviations are used in Eqn. 2:

$$A_1 = \mu\phi\sin(\theta) - \beta\left(1+\cos(\theta)\right)$$

$$A_2 = \mu\left(\theta\cos(\theta) - \sin(\theta)\right)$$

$$A_3 = -\beta\left(\theta - \sin(\theta)\right) - A_2$$

$$A_4 = \mu\theta\cos(\theta) + \frac{1}{2}(1-\beta)\sin(\theta)$$

$$A_5 = -\mu\theta sin(\theta)$$

$$A_6 = \frac{1}{2}(1-\beta)\sin(\theta) - \mu\theta\cos(\theta)$$

$$\beta = \frac{EI}{GK}$$

$$\mu = \frac{1}{2}(1+\beta)$$

$$R = \frac{1}{2}(R_o + R_i)$$

$$b = R_o - R_i$$

$$c_2 = 0.0347\left(\frac{b}{t}\right)^2 - 0.2303\left(\frac{b}{t}\right) + 0.3353$$

$$K = c_2 b t^3$$

$$I = \frac{1}{12} b t^3$$

In these equations, R_o denotes the outer and R_i the inner radius of the spring arm. Its thickness is denoted by t, see Fig. 12. The angle θ used in these equations differs from the nominal angle φ: Whereas the nominal angle φ (see Fig. 4) refers to the center lines of spacer and slider, the free angle θ refers only to the part of the spring arm outside the clamping regions, see Fig. 4. With the used specimen dimensions (see Fig. 3) the difference between the free angle θ and the nominal angle φ is given in Eqn. 3.

$$\theta = \varphi - 8.4° \tag{3}$$

The stiffness contribution of the spacer k_s is analysed by FE analysis of the system consisting of spring arm, spacer and slider shown in Fig. 4 for the case of a spring arm with a thickness of t = 3 mm and spacers of the same thickness.
Fig. 13 depicts the axial stiffness of the spring arm computed by the analytical approach according to Eqn. 2 (-) and the corresponding stiffness values computed by the FE model (+) for a configuration with a spring arm and spacer thickness of t = 3 mm and three spacer arms.
Whereas the clamping by the slider can be considered approximately as rigid, this is not the case for the clamping by the spacers. Hence, it is assumed that the difference between the ideal and the computed stiffness is mainly due to the clamping stiffness of the spacer k_s. The spacer allows the end of the spring arm to rotate around both the radial and tangential axes. The contributions of these two degrees of freedom to the overall deformation can be represented by a linear dependence of the additional compliance on the distance of the slider from the respective axes of rotation, h_B rsp. h_T, see Fig. 4 and Eqn. 4.

$$k_s = 1 / \left(\frac{h_T}{C_{s,T}} + \frac{h_B}{C_{s,B}}\right) \tag{4}$$

$$h_B = R\sin(\theta)$$

$$h_T = R\left(1 - cos\left(\theta\right)\right)$$

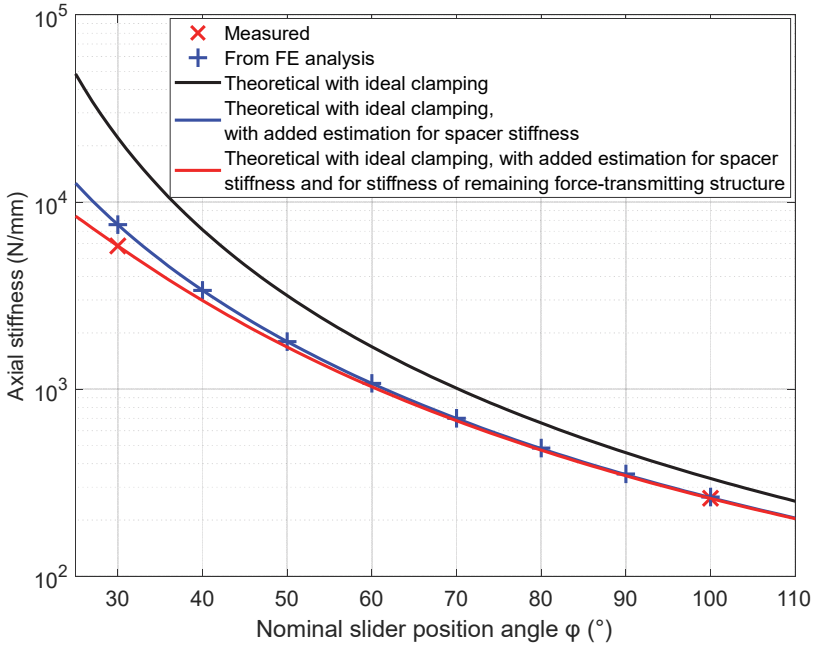

Figure 13: Measured and computed (FE) stiffness together with the approximation approach.

Other orders of the parameters h_T and h_B result in a less accurate approximation of the FE results. Fig. 13 depicts the resulting approximation with $C_{s,T}$ = 83 904 N and $C_{s,B}$ = 522 784 N (for three spacer arms) (-) showing a good correlation with the numerical results. This curve corresponds to Eqn. 1 with $1/k_{fts} = 0$. The stiffness values measured in the experiments for this geometry (see Tab. 2) are depicted in Fig. 13, too (X). For the nominal angle of φ = 100° the measured value is only 1.5% lower than the one computed by FE, but for the angle of φ = 30° the measured stiffness is 23% lower than the stiffness computed by FE. It can be assumed that the difference is attributed to the stiffness of the remaining force-transmitting structure, which can be calculated directly from the difference using Eqn. 1. This results in k_{fts} = 25 311 N/mm. The stiffness approximation according to Eqn. 1 with this value is depicted in Fig. 13, too (-).

The stiffness approximation for the ideal spring arm k_{sa} in Eqn. 2 is valid for a wide variety of geometries, but the ones for the stiffness contribution of the spacer k_s and of the other force transmitting structures k_{fts} are only valid for the geometry under investigation in this study. The impact of k_{fts} is negligible for soft configurations with thin spring arms and/or large slider position angles φ and moderate for the stiffest configuration in the investigation with φ = 30° and t = 3 mm. Thus, it is acceptable to use an experience-based estimation for this parameter. But the approximation for the spacer-related stiffness contribution k_s needs to be extended to a larger range of dimensions. To investigate the dependence of the spacer stiffness on the sheet thickness, this parameter was varied in the FE model (see Fig. 4) for the two angles φ = 30° and φ = 100°. It is assumed that the spacer thickness equals the thickness t of the spring arm. This limitation facilitates the fabrication of spacers and spring arms from a singular semi-finished sheet metal product. The result is shown in Fig. 14, where the spacer stiffness k_s was determined from the total stiffness k_{tot} calculated in the FE model using Eqn. 1 (with $1/k_{fts} = 0$, because this stiffness contribution is not included in the FE model) and Eqn. 2.

The extended estimation for the spacer stiffness k_s using a 2nd order approach for the thickness dependence as given in Eqn. 5 is depicted in Fig. 12, too.

$$k_s = \left(\frac{t}{t_{ref}}\right)^2 / \left(\frac{h_T}{C_{s,T}} + \frac{h_B}{C_{s,B}}\right) \tag{5}$$

$t_{ref} = 3\,\text{mm}$

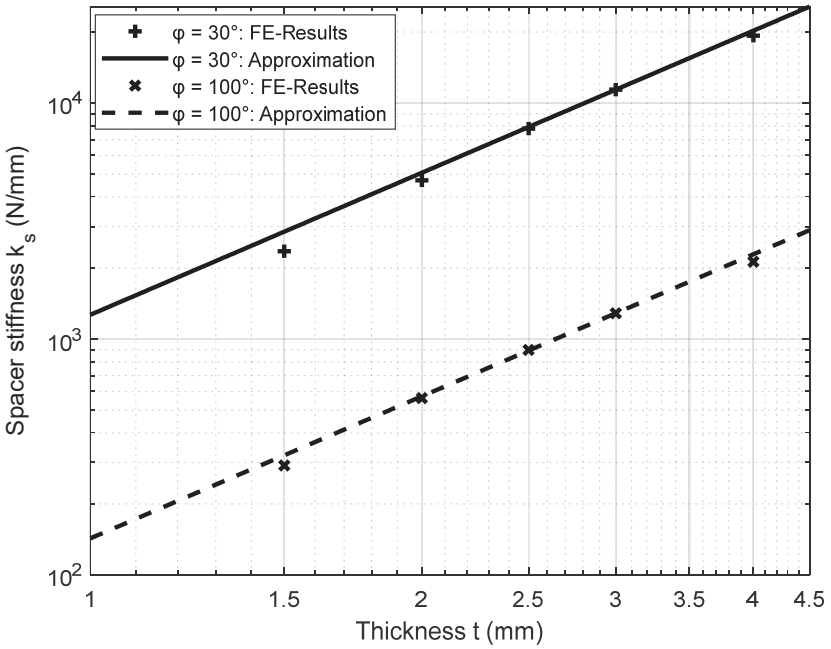

Figure 14: Dependence of spacer stiffness on sheet thickness t based on FE analysis.

In this equation t_{ref} denotes the reference thickness for which the parameters $C_{s,T}$ and $C_{s,B}$ have been determined. If the dimensions of an arbitrary geometry are scaled proportionally in all spatial directions, the general rule is that the translational stiffness also increases linearly with the scaling factor. Eqn. 5 complies with this rule. Therefore, this equation is suitable for geometries of spacers and spring arms with the same aspect ratios of all dimensions, which are perpendicular to the thickness direction. If the spring arm radius R is changed moderately while the spring arm width b remains constant, the impact on the spacer geometry is rather small. Hence, it can be assumed that the effect on the spacer stiffness is predominantly due to the changes of the lever arms h_B and h_T, which is included in Eqn. 5. For such a geometry with modified radius the same scaling rules regarding thickness and proportional scaling of all dimensions apply. Therefore, it can be assumed that Eqn. 5 also holds approximately for geometries with moderately different ratios of spring arm radius R and spring arm width b. However, the impact of this ratio wasn't in the focus of investigations of this study, hence Eqn. 5 should be used with care for geometries, for which the ratio differs significantly from the ratio $R/b = 4.5$ used here.

Notch stress estimation approach for quick fatigue strength approximation

For notch stress estimation, two different approaches are used: The first approach enables a quick estimation of the influence of the geometric parameters on the fatigue strength properties without FE analysis and thus an efficient automated parameter optimization. The second approach presented in the following paragraph is used for FE-based fatigue strength evaluation.

The approximation of fatigue strength for a quick preliminary design of the stiffness elements is based on FE parameter studies. It is not intended to replace the FE-based fatigue strength assessment of the geometry, but to enable developers to quickly derive an approximation of the required dimensions of the stiffness elements for given stiffness and load requirements.

In general, the geometry of the tunable stiffness device has many geometric parameters. For the quick fatigue strength approximation only three parameters shall be used: the spring arm thickness t, the spring arm width b and the notch radius r. The spring arm radius R is considered only indirectly by its impact on the moments in the spring arm. This restriction

requires that all other geometric parameters are determined as a function of these three parameters. For the spacer, the dependency is chosen in such a way that the spacer radius r_s (see Fig. 3) is proportional to the width of the spring arm b. As with the stiffness approximation in the previous section, it is assumed that the spacer thickness equals the thickness t of the spring arm. The following approximation for the fatigue strength applies only to spacer geometries, which comply with these geometrical rules.

In general, if a moment-loaded geometry is scaled proportionally in all dimensions, the stresses will decrease with the third power of the scaling factor, if the moment remains constant. A quadratic relationship is assumed for the dependence of stresses on the thickness, analogous to the section modulus for bending and torsion of beams with thin rectangular cross section. Based on these prerequisites, the correlation given in Eqn. 6 is proposed for a simplified stress approximation.

$$\sigma_{Pseudo,ii} = \left(\frac{t_{ref}}{t}\right)^2 \left(\frac{r_{ref}}{r}\right)\left(M_B f_{B,ii}\left(\frac{b}{r}\right) + M_T f_{T,ii}\left(\frac{b}{r}\right)\right) \tag{6}$$

$$t_{ref} = 1\,\text{mm}$$

$$r_{ref} = 1\,\text{mm}$$

In this equation, ii denotes the index of the individual stress components. The functions $f_{B,ii}$ and $f_{T,ii}$ indicate the stress at a moment of 1 Nmm as a function of the ratio of the spring arm width b and the notch radius r for each stress component. To be able to find an approximation of these functions, a parameter study was carried out with the FE model of a straight spring arm ($R = \infty$), which is shown in Fig. 15.

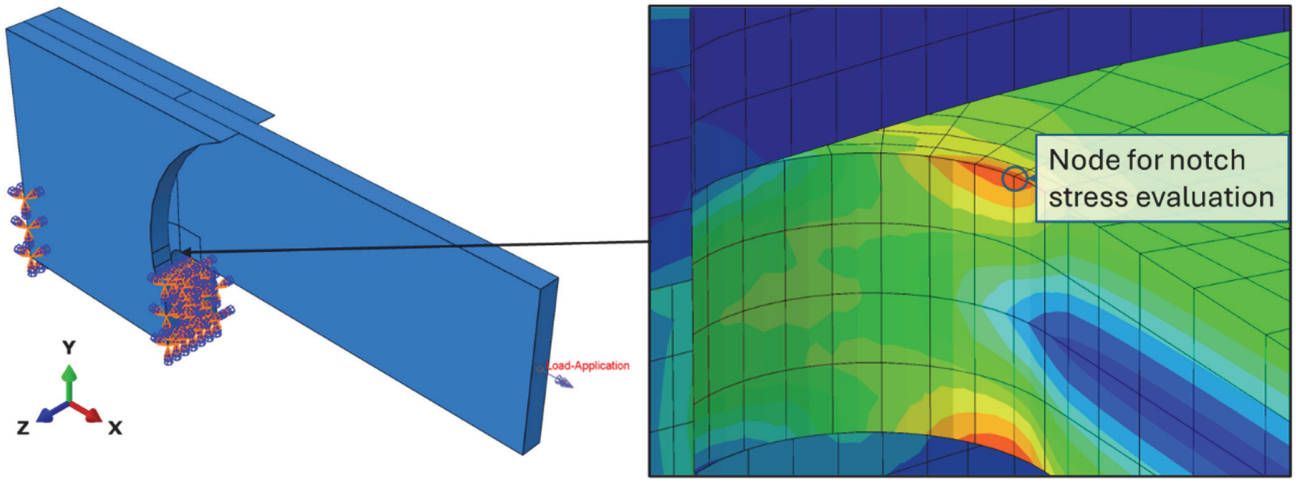

Figure 15: FE model to analyse the correlation between the ratio b / r and the notch stresses (left) and selected node for stress evaluation (right).

At the end of this straight spring arm, either a torsional or a bending moment was applied. The spring arm width was varied for two different spring arm thicknesses: for t = 1.5 mm, widths from 4.5 to 17.9 mm were analysed, and for t = 3 mm, widths from 4.5 to 35.7 mm were analysed. In each case, there is a factor of 1.29 between two neighboring width values. As shown in Fig. 5, the most critical location for failure of the spring arm is at the notch radius between the spring arm and the inner ring. Therefore, for dimensioning the stiffness device it is essential to estimate the material- and geometry-related critical stress for fatigue at this location. The selected node for notch stress evaluation is marked in Fig. 15. Fig. 16 shows the derived stress estimation functions for bending $f_{B,ii}$ and torsion $f_{T,ii}$ together with the supporting values from the FE study.

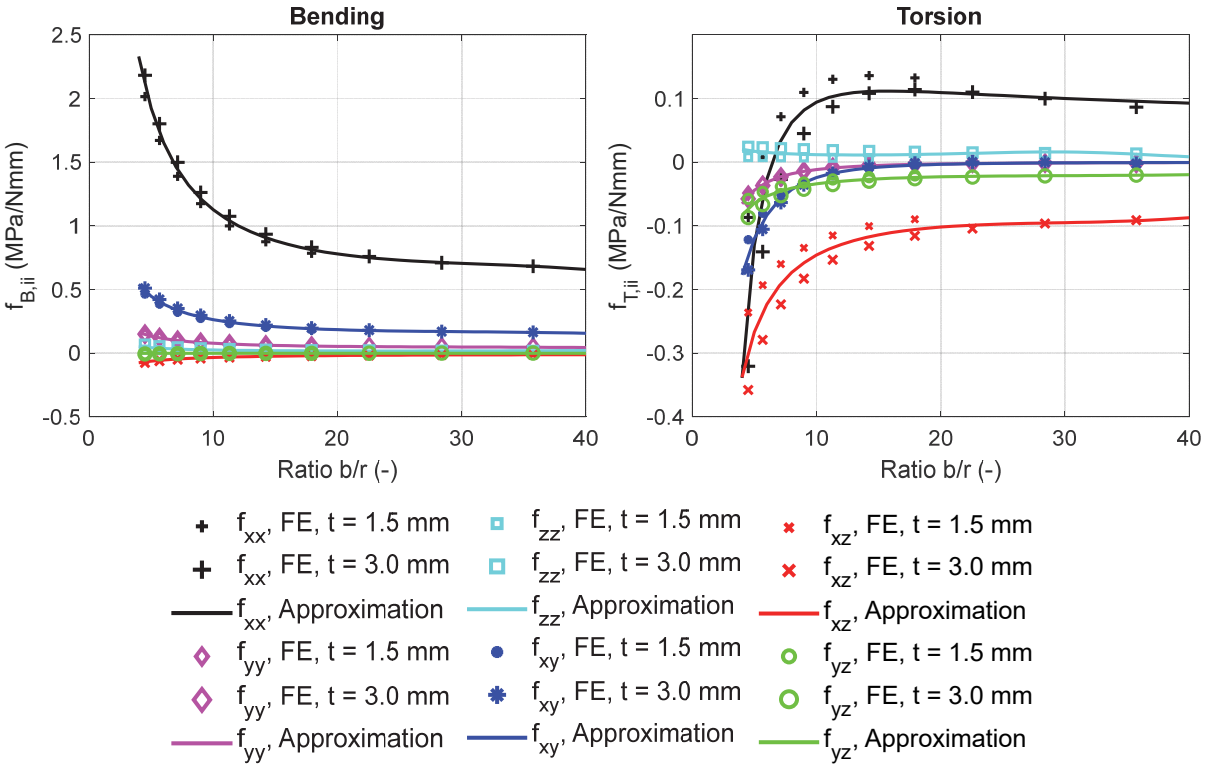

Figure 16: Stress estimation functions for bending $f_{B,ii}$ (left) and torsion $f_{T,ii}$ (right) for stresses at the notch based on the FE sensitivity study.

The supporting values derived from the model with t =3 mm and with t = 1.5 mm are not identical for the same width values, because the scaling rule used in Eqn. 6 is only an approximation. The highest relative differences occur for torsion of spring arms with a small width b. Furthermore, it should be mentioned that the stress components $\sigma_{pseudo,yy}$, $\sigma_{pseudo,zz}$ and $\tau_{pseudo,yz}$ at the evaluation location are not equal to zero only because they are calculated according to the FE method at the integration points inside the elements and not directly at the edge. For most of the stress components the approximation given in Fig. 16 is derived by a least-squares fit of the polynomial function given in Eqn. 7. For $f_{T,xx}(b/r)$ a different approximation function is used, which is given in Eqn. 8. $f_{B,yz}(b/r)$ is neglected ($f_{B,yz}(b/r)=0$).

$$f_{ii}\left(\frac{b}{r}\right)=\frac{1}{p_3\left(\frac{b}{r}\right)^3+p_2\left(\frac{b}{r}\right)^2+p_1\left(\frac{b}{r}\right)+p_0} \tag{7}$$

$$f_{T,xx}\left(\frac{b}{r}\right)=\frac{1}{p_3\left(\frac{b}{r}\right)^3+p_2\left(\frac{b}{r}\right)^2}-\frac{1}{p_1\left(\frac{b}{r}\right)}+\frac{1}{p_0} \tag{8}$$

In Tab. 3, the parameters are listed which were used in these equations for the approximations shown in Fig. 16.

	p_3 (Nmm/MPa)	p_2 (Nmm/MPa)	p_1 (Nmm/MPa)	p_0 (Nmm/MPa)
		Bending		
$f_{B,xx}$	3.86E-05	-3.62E-03	1.21E-01	0
$f_{B,yy}$	5.69E-04	-5.26E-02	1.75E+00	0
$f_{B,zz}$	1.29E-03	-1.57E-01	5.39E+00	0
$f_{B,xy}$	1.78E-04	-1.63E-02	5.24E-01	0
$f_{B,xz}$	5.46E-04	-3.05E-03	-2.82E+00	-2.03E+00
$f_{B,yz}$	-	-	-	-
		Torsion		
$f_{T,xx}$	4.70E-04	-7.75E-02	-5.86E-01	1.65E+01
$f_{T,yy}$	-1.27E-02	-6.21E-01	-1.13E+00	0
$f_{T,zz}$	1.33E-02	-8.48E-01	1.55E+01	0
$f_{T,xy}$	-3.93E-02	9.60E-02	-1.17E+00	0
$f_{T,xz}$	-4.15E-04	3.62E-02	-1.09E+00	8.51E-01
$f_{T,yz}$	-1.60E-03	1.47E-01	-4.70E+00	4.52E+00

Table 3: Parameters used for the approximation of the notch stress components with Eqn. 7 and Eqn. 8.

Using the approximation in Eqn. 6 together with these functions, estimation of the moments M_B and M_T is required. For this strength approximation approach, the moments for the case with rigid clamping at the end are assumed, even though the clamping by the spacers is not really rigid. With this simplification Eqn. 9 to Eqn. 12 provide the moments.

$$M_T = M_{B,slider}\,\sin(\phi) + M_{T,slider}\cos(\phi) - FR\left(1-\cos(\phi)\right) \tag{9}$$

$$M_B = M_{B,slider}\,\cos(\phi) - M_{T,slider}\sin(\phi) - FR\left(\sin(\phi)\right) \tag{10}$$

$$M_{B,slider} = FR\frac{A_2}{A_5} - T_A\frac{A_6}{A_5} \tag{11}$$

$$M_{T,slider} = FR\frac{\frac{A_1}{A_5} - \frac{A_2 A_4}{A_5^2}}{1-\left(\frac{A_6 A_4}{A_5^2}\right)} \tag{12}$$

$M_{B,slider}$ and $M_{T,slider}$ denote the corresponding moments at the slider end of the spring arm. See Eqn. 2 for the abbreviations A_1 to A_6. Because the derivation of this approximation is based on mechanical considerations with simplified assumptions regarding geometry and boundary conditions in Eqn. 2 and Eqn. 9 - 12, no exact agreement with the notch stresses according to an FE analysis of the actual geometry can be expected. Rather, the stress values determined are to be regarded as pseudo-stresses that cannot be directly compared with the S-N curve in Fig. 11. Instead, a separate S-N curve is determined for this pseudo-stress by determining the associated Mises pseudo-stress value, Eqn. 13, for the individual sample tests and using this as the basis for determining a new pseudo-stress S-N curve, which is shown in Fig. 17.

$$\sigma_{Pseudo,Mises} = \sqrt{\sigma_{xx}^2 + \sigma_{yy}^2 + \sigma_{zz}^2 + 3\left(\tau_{xy}^2 + \tau_{xz}^2 + \tau_{yz}^2\right)} \tag{13}$$

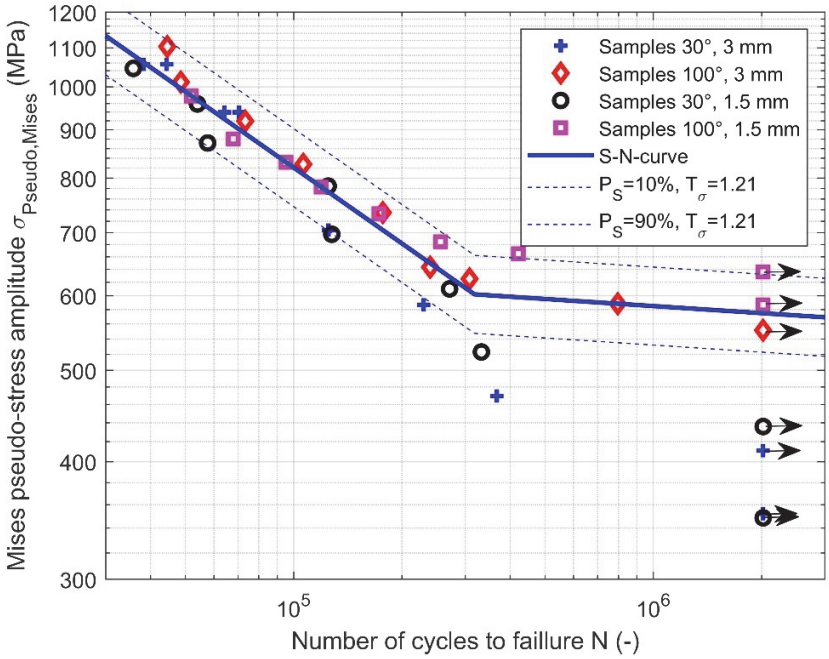

Figure 17: S-N curve for Mises pseudo-stresses derived in the proposed approximation approach.

The S-N curve depicted in this figure has an inclination of k = 3.74, a knee-point of N_k = 318 000 cycles and a stress amplitude at the knee-point of σ_k = 602.1 MPa. 80% of the samples are within a scatter band with a width of T_σ = 1.21, but individual samples failed at values that were up to 1.28 times lower than the S-N curve. Extrapolation to dimensions significantly different from the ones under investigation in the tests used for calibration here should be done with caution. However, together with the stiffness estimation in the previous section, this approximation offers the possibility to quickly estimate the required dimensions of spring elements for given stiffness and strength requirements.

CONCLUSIONS

Tunable mounts are a promising technology for adapting system dynamics as well as for flexible tests on components and substructures. In all these applications, these devices are exposed to cyclic loading. This study investigated the fatigue properties and stiffness behavior of a tunable spring element made from C85S+QT sheet steel, intended for use in mounts with adjustable stiffness. Through experimental fatigue tests S-N curves for four different configurations, varying in sheet thickness and slider angle, were established. The experimental results provide necessary information on the fatigue strength of the mounts, defining the limits for their safe usage. The results show that the fatigue life of the mounts is strongly dependent both on the sheet thickness and the slider angle. Most failures occurred at the notch between the spring arm and the inner ring, highlighting this area as the critical location for fatigue assessment.

Analytical approximations for a quick estimation of both stiffness and fatigue strength are proposed. They are calibrated based on experimentally determined stiffness values and fatigue lives together with numerical parameter studies. The proposed estimations allow for a quick estimation of stiffness and fatigue strength based on the geometric parameters slider angle, spring arm thickness, spring arm width and notch radius. These estimations allow to inter- and extrapolate the experimental results to other geometries using only analytical equations for computing the stiffness and a pseudo-stress amplitude, which can be compared to the derived pseudo-stress S-N curve. This allows for a quick pre-dimensioning of the mounts based on strength and stiffness requirements. The proposed approximation can be used by interactive tools or scripts to provide immediate feedback to the designer regarding the effect of geometrical modifications and may be integrated into automated design optimization algorithms. However, this pre-dimensioning does not replace a more accurate FE-based fatigue strength assessment.

The FE-based models provide more accurate predictions and can be used for final design validation, especially when the geometry deviates from the tested configurations. Such an assessment can be performed using the derived geometry and

material related S-N curve for the notch stress at the spring arm, which was derived in this paper using FE based stress analysis of the fatigue tests.
A key outcome is the development of a practical design workflow: initial dimensioning can be performed using the provided analytical formulas and S-N curves for pseudo-stresses, while final validation should rely on FE-based notch stress analysis and the corresponding S-N curve. This approach ensures that mounts can be reliably designed to meet both stiffness and durability requirements, supporting their use in dynamic system adaptation and flexible test setups.

REFERENCES

[1] Guiggiani, M. (2023). The Science of Vehicle Dynamics, Cham, Springer. DOI: https://doi.org/10.1007/978-3-031-06461-6.

[2] Hamann, T., Hansen, S., Bitterolf, D., Boehlmann, C., Moeller, C., Seifried, R. and Hintze, W. (2022). Experimental analysis of a hybrid drive train implemented in a novel industrial robot approach. ISR Europe 2022; 54th International Symposium on Robotics, Munich, Germany, pp. 1–8.

[3] Infante, F., Kaal, W., Perfetto, S. and Herold, S. (2018). Design development of rotational energy harvesting vibration absorber (R-EHTVA). ASME 2018 Conference on Smart Materials, Adaptive Structures and Intelligent Systems (SMASIS), San Antonio, TX, USA. DOI: https://doi.org/10.1115/SMASIS2018-7902

[4] Reis, M. and Tüfekci, K. (2023). A variable clutch mechanism for adjustable stiffness actuators based on bending and torsion of prismatic beams. Actuators, 12(1), p.8. DOI: https://doi.org/10.3390/act12010008.

[5] Shen, X., Yu, C., Guo, R., et al. (2025). Controlling the longitudinal vibration of an elastic rod within a wide frequency band by utilizing an adjustable stiffness internal support. Chinese Journal of Mechanical Engineering, 38, p.99. DOI: https://doi.org/10.1186/s10033-025-01253-3

[6] Aktaş, B. (2021). Multidimensional Tunable Mechanics Using Jamming. Doctoral dissertation, Harvard University Graduate School of Arts and Sciences.

[7] Jafari, A., Tsagarakis, N.G. and Caldwell, D.G. (2011). AwAS-II: A new actuator with adjustable stiffness based on the novel principle of adaptable pivot point and variable lever ratio. 2011 IEEE International Conference on Robotics and Automation, Shanghai, China, pp. 4638–4643. DOI: https://doi.org/10.1109/ICRA.2011.5979994.

[8] Markuszewski, D., Wądołowski, M. and Krajewski, A. (2024). The influence of variable stiffness of the shape memory alloys carbon composite structure on mechanical vibration. Materials, 17(2), p.480. DOI: 10.3390/ma17020480.

[9] Hao, Y.T., Gao, J.Y., Lv, Y.G. and Liu, J. (2022). Low melting point alloys enabled stiffness tunable advanced materials. Advanced Functional Materials, 32, 2201942. DOI: https://doi.org/10.1002/adfm.202201942.

[10] Yazdani Sarvestani, H., Beausoleil, C., Genest, M. and Ashrafi, B. (2020). Architectured ceramics with tunable toughness and stiffness. Extreme Mechanics Letters, 39, 100844. DOI: https://doi.org/10.1016/j.eml.2020.100844.

[11] Yang, S., Wang, P., Liu, Y., Dong, X., Tong, Y. and Zhao, Y. (2021). Modified Bouc-Wen model based on fractional derivative and application in magnetorheological elastomer. Frontiers in Materials, 8. DOI: https://doi.org/10.3389/fmats.2021.743716.

[12] Saxena, A., Manogharan, G. and Rahn, C. (2025). Adaptive stiffness structures via additively manufactured fluid accumulators, Smart Materials and Structures, 34, 015055. DOI: https://doi.org/10.1088/1361-665X/ada09b.

[13] Biere, A. (2017). Entwicklung einer Methodik zur experimentellen Qualifizierung von Bolzensetzverbindungen unter Berücksichtigung dynamischer Effekte, Berichte aus dem Laboratorium für Werkstoff- und Fügetechnik, 131, Aachen, Shaker Verlag. ISBN: 9783844054897.

[14] Millitzer, J., Hansmann, J., Lapiccirella, G., Song, D. and Kang, Y.J. (2022). High-bandwidth mechanical hardware-in-the-loop emulation of structural dynamics for more efficient NVH development and testing. 12th International Styrian Noise, Vibration & Harshness Congress: The European Automotive Noise Conference, Graz, Austria. DOI: https://doi.org/10.4271/2022-01-0953.

[15] Landersheim, V., Wallmichrath, M. and Möller, R. (2025). Efficient strength testing of substructures of agricultural vehicles. Agricultural Engineering.EU, 80(2). DOI: https://doi.org/10.15150/ae.2025.3334.

[16] Landersheim, V., Hansmann, J., Wallmichrath, M., Zinke, R., Chéreau, S., Bruder, T. and Bilger, F. (2024). Methode zur Betriebsfestigkeitsprüfung strukturintegrierter Hochvoltspeicher mittels eines multiaxialen Schwingtischs. DVM Conference: Betriebsfestigkeit – Betriebsfestigkeit nicht mehr relevant? – oder der Schlüssel für eine sichere und nachhaltige Zukunft!, Clausthal-Zellerfeld, Germany, 9-10 October. DOI: https://doi.org/10.48447/BF-2024-424.

[17] Kloos, K.H., Buch, A. and Zankov, D. (1981). Pure geometrical size effect in fatigue tests with constant stress amplitude and in programme tests. Materialwissenschaft und Werkstofftechnik, 12(2), pp. 40–50.

DOI: https://doi.org/10.1002/mawe.19810120205.
[18] Siebel, E. and Stieler, M. (1955). Ungleichförmige Spannungsverteilung bei schwingender Beanspruchung. VDI-Zeitschrift, 97(5), pp. 121–126.
[19] Sonsino, C.M. (1993). Zur Bewertung des Schwingfestigkeitsverhaltens von Bauteilen mit Hilfe örtlicher Spannungen. Konstruktion, 45(1).
[20] Weibull, W. (1939). The phenomenon of rupture in solids. Proceedings of the Royal Swedish Institute of Engineering Research, 153.
[21] Young, W.C., Budynas, R.G. and Sadegh, A.M. (2011). Roark's Formulas for Stress and Strain, 8th ed., New York, McGraw Hill. ISBN: 9780071742474.